Correlative Imaging of Structural Biochemistry in Plant and Food Quality Research Within an Interoperable Data Acquisition Platform

Marjana Regvar, Boštjan Jeni, Martin Šala, Aleš Kladnik, Iztok Dogša, Maja Koblar, Mitja Kelemen, Primož Vavpeti, Katarina Vogel-Mikuš, Ivan Kreft, Primož Pelicon, Paula Pongrac

Microscopy and Microanalysis, 2025, **31**, ozaf057
https://doi.org/10.1093/mam/ozaf057
Advance access publication 15 July 2025
Original Article

Microscopy AND Microanalysis

Correlative Imaging of Structural Biochemistry in Plant and Food Quality Research Within an Interoperable Data Acquisition Platform

Marjana Regvar[1], Boštjan Jenčič[2], Martin Šala[3], Aleš Kladnik[1], Iztok Dogša[1], Maja Koblar[2], Mitja Kelemen[2], Primož Vavpetič[2], Katarina Vogel-Mikuš[1,2], Ivan Kreft[4], Primož Pelicon[2], and Paula Pongrac[1,2,*]

[1]*Biotechnical Faculty, University of Ljubljana, Jamnikarjeva ulica 101, SI-1000 Ljubljana, Slovenia*
[2]*Jožef Stefan Institute, Jamova cesta 39, SI-1000 Ljubljana, Slovenia*
[3]*National Institute of Chemistry, Hajdrihova ulica 19, SI-1000 Ljubljana, Slovenia*
[4]*Nutrition Institute, Koprska ulica 98, SI-1000 Ljubljana, Slovenia*

***Corresponding author:** Paula Pongrac, E-mail: paula.pongrac@bf.uni-lj.si

Abstract

Correlative imaging is a powerful tool for revealing information on cell-type structures and their biochemistry, with the potential to inform healthier food choices and improved dietary recommendations. Determination of plant structures and their structural biochemistry advances our understanding of specific structures designed to store different biomolecules within cells and tissues. Compared to the classical biochemical separation techniques, the key advantage of sequential correlative imaging techniques is in relating spatial plant (micro)structures to their biochemistry in a nondestructive manner. Sequential imaging reported here comprises six methodologies on a single sample, a cross-section of a Tartary buckwheat (*Fagopyrum tataricum*) grain, namely, bright-field and autofluorescence microscopy, fluorescence microspectroscopy, MeV-secondary ion mass spectrometry, micro-particle-induced X-ray emission, scanning electron microscopy coupled with energy dispersive X-ray spectroscopy, and laser ablation-inductively coupled plasma-mass spectrometry. Results confirm that the stepwise addition of the desired information across several classes of biomolecules and several spatial scales informs the quality and safety of plant-based produce across scales. Therefore, a viable workflow is proposed, enabling sequential spatial analysis of grain and highlighting plant structures' in situ specificity. The advantages and disadvantages of the selected methodologies were critically evaluated.

Key words: autofluorescence, correlative molecular imaging, element distribution, *Fagopyrum tataricum*, grain tissues, Tartary buckwheat

Graphical Abstract

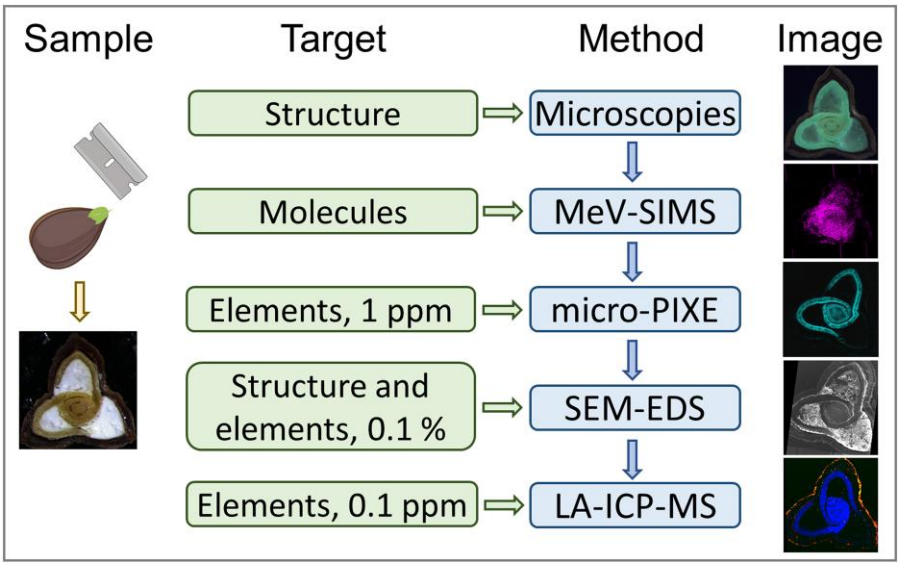

Received: January 13, 2025. **Revised:** May 2, 2025. **Accepted:** June 13, 2025

Introduction

Plants are the basis of our diets, providing vital sources of energy-rich compounds, mineral nutrients, vitamins, essential amino and fatty acids, and a plethora of bioactive compounds beneficial to our health and well-being (Eckardt, 2011; White et al., 2013). Food crop quality, however, is a highly complex concept due to a large number of plant characteristics and the various genetic and exogenous factors that control them (Murphy et al., 2011). While the cultivation of new, high-yielding crop varieties, along with the increasing use of mineral fertilizers and crop protection chemicals, resulted in an enormous increase in crop yields, little attention was paid to the nutritional quality and safety of food crops (White & Broadley, 2005; Murphy et al., 2008; Mayer et al., 2022; Miner et al., 2022). Furthermore, multiple environmental challenges of the 21st century, including climate change, environmental pollutants, and shifting population demographics, threaten global food sustainability and nutrition security. Therefore, innovative solutions must be developed to inform decisions across the food chain toward improved nutritional and health status of plant-based foods (Khoo & Knorr, 2014). Notwithstanding the importance of plants as a source of exploitable and essential biochemicals, we still have remarkably limited knowledge of where these metabolites are produced and stored within plants, presumably due to the scarcity of suitable analytical tools allowing the determination of their localization within organs and tissues (Etalo et al., 2015).

A single analytical technique cannot capture the detailed structural biochemistry of a complex biological (Walter et al., 2020, 2021) or soil (Lippold et al., 2023) sample. Therefore, coupling different imaging techniques, preferably on different spatial scales, known as the correlative imaging workflow to visualize and relate comprehensive plant spatial biochemical composition to plants' anatomical, physiological, and genetic traits needs to be developed. Such integrative research has the potential to advance biomedical and plant sciences, although, in the latter, it is much less routinely practiced (Jahn et al., 2012) due to complex sample preparation demands and potential sample damage induced by the imaging technique(s) applied. Integrating bright-field microscopy (BFM), fluorescence microscopy (FM) and electron microscopy (EM), mass spectrometry imaging (MSI), and elemental spatial-resolution imaging (ESRI) techniques for detailed analysis of biological samples offers the potential to simultaneously reveal information on plant tissues and their biochemical and elemental compositions in a spatially resolved manner. The integration of all these techniques holds great potential to become the next-generation bioimaging strategy and represents an innovative analytical approach in plant and food science comparable to zoology and medicine (Zhao et al., 2021). Among those, microscopies such as BFM and EM are readily and routinely used techniques to capture the morphology of a sample at the micro- and nanoscale, respectively. When EM is coupled with an energy dispersive X-ray spectrometer (EDS), the relationship between plant ultrastructure and their elemental composition is determinable, but with sensitivity in 0.1% concentration range, exemplified by demonstrating the importance of plant cuticles, stomata, trichomes, and overall foliar surface free energy on the adhesion, uptake, and translocation of metal nanoparticles in plants (da Silva et al., 2006; Schreck et al., 2012; Kranjc et al., 2018). By contrast, MSI and ESRI are less easily accessible and require extensive operational and sample preparation skills. Of MSI available, recently developed secondary ion MSI using heavy ions with MeV energy (MeV-SIMS) provides information on the mass-to-charge (m/z) ratio of molecules and molecular fragments in a plant sample with a high yield and spatial resolution (Nakata et al., 2008; Jenčič et al., 2019). A close relationship between plant metabolites and specific plant tissues (structures) has been demonstrated on a cannabis leaf (Jenčič et al., 2016). However, despite the tremendous progress in MS-based metabolomics platforms, metabolite annotation and identification remain a bottleneck (Hamany Djande et al., 2020). Among ESRI, micro-particle Induced X-ray emission (micro-PIXE) provides information on the presence and location of an extensive range of elements (sodium to uranium) in both freeze-dried and frozen-hydrated states (Vogel-Mikuš et al., 2008; Vavpetič et al., 2015). Quantitative distribution maps enable correlating elemental composition to specific plant structures. For the elements present in trace and ultratrace concentrations (e.g., $<1\ \mu g\ g^{-1}$) such as mercury (Hg), cadmium (Cd), arsenic (As), and selenium (Se) (Nielsen, 1984), better sensitivity is required; therefore, synchrotron radiation micro-X-ray fluorescence-based spectrometry and laser ablation inductively coupled mass spectrometry (LA-ICP-MS) are better choices, also when imaging distribution of low Z elements present in low concentration in plants, such as aluminum (Al) and silicon (Si) (Yamaji & Ma, 2019) are required. In addition, Se and As can also be determined using nano-SIMS (Moore et al., 2011).

One of the main challenges in correlative imaging is preventing damage to the sensitive biological tissues during imaging and optimizing the sequence of analyses to avoid misinterpretation due to potential artifacts. Optimization of the methodology sequence must ensure that the subsequent techniques are "blind" to the potential artifacts occurring in the previous analyses. Therefore, the sequence should begin with the least damaging to the most damaging analytical technique (Costa et al., 2022). In addition, the sample preparation protocol must ensure the preservation of structural and biochemical features in vivo to the highest degree possible (Vogel-Mikuš et al., 2014). To demonstrate the advantage of correlative imaging information for plant and food quality and composition, we applied six consecutive techniques in the following order: BFM, FM, MeV-SIMS, micro-PIXE, SEM-EDS, and LA-ICP-MS to a single section of Tartary buckwheat (*Fagopyrum tataricum*) grain. Tartary buckwheat is a gluten-free crop with numerous health-promoting effects, whose grain has a distinctive morphology with a tissue-specific element profile (Pongrac et al., 2013). Its health-beneficial effects comprise prebiotic and antioxidant activities, anti-inflammatory and antidiabetic effects, reduction in cholesterol levels, and improvements in hypertension conditions, as well as neuroprotection and anticancer activity (Giménez-Bastida & Zieliński, 2015). Rutin represents 90% of the flavonoids and is one of the key antioxidants in Tartary buckwheat grain, although quercetin and isoorientin are also present (Morishita et al., 2007; Lee et al., 2016). Rutin and resistant starch are linked to attenuated oxidative stress of the liver and small intestine and are among the compounds by which Tartary buckwheat extracts contribute to the beneficial effects of whole grain foods (Luo et al., 2019). Still, the visual confirmation of the microstructures of the Tartary buckwheat grain tissues containing the most effective biomolecules and their allocation within the grain is lacking. Therefore, a method development approach was performed

using a sequence of six techniques to meaningfully capture the spatial biochemistry of a sample, namely, Tartary buckwheat grain. When performed on the cryo-preserved dehydrated plant specimens, the proposed sequential imaging workflow can be applied to a wide variety of plant specimens and has the potential to fill the gap in our knowledge of structural plant biochemistry across scales, in situ, e.g., with no chemical alterations in a nondestructive manner. The imaging setups used are available within the Slovenian Correlative Bioimaging Node (SiMBION), a partner of the Euro-BioImaging platform (https://www.eurobioimaging.eu/), which is dedicated to all aspects of imaging. The nodes of Euro-BioImaging provide open access to biomedical and biological imaging technologies and training on the optimized sample preparation techniques, the proper handling of state-of-the-art technologies, and data analysis, thus bridging the specific challenges of interdisciplinary research (Pfander et al., 2022).

Material and Methods

Sample Preparation

Grain of Tartary buckwheat (*F. tataricum* [L.] Gaertn.) cv. Zlata from the 2019 harvest was obtained from a local farm and mill Rangus (Rangus Mlinarstvo in trgovina, Dol. Vrhpolje d.o.o., Dolenje Vrhpolje 15, 8310 Šentjernej, Slovenia). Between harvest and use, the grain was kept in closed glass jars in a dry and dark place at room temperature. On the day of sample preparation, grains were soaked in precooled Milli-Q at 4°C for 4 h and cut transversely using a sharp stainless-steel platinum-coated razor blade (Science Services, Germany). Sections were carefully packed between several layers of tin foil (to ensure the flatness of sections) and plunge-frozen in liquid nitrogen and freeze-dried (Alpha 2-4 Christ, Martin Christ Gefriertrocknungsanlagen GmbH, Osterode am Harz, Germany) for 3 days at 0.012 mbar and −40°C (Supplementary Fig. 1). Dried sections were inspected under the stereomicroscope (Leica MZ8, Leica Camera AG, Wetzlar, Germany) and those with intact embryonic axis and outer layers (i.e., pericarps) present were selected, placed on double-sided carbon tape (SPI Supplies, USA) on polished Si wafer (Sitronic AG, München, Germany), and kept in glass Petri dishes until analyses. Three independent Tartary buckwheat grain sections were analyzed using the sequence of six imaging methods described below, selected based on their basic characteristics, performance, advantages, and disadvantages summarized in Table 1.

Correlative Sample Imaging

Morphology of the grain was imaged using BFM and FM, followed by molecular imaging (MeV-SIMS), element distribution imaging at micrometer scale (micro-PIXE), morphology and element distribution imaging below micrometer scale (SEM-EDS), and element distribution imaging for elements present at low concentrations (LA-ICP-MS).

BFM and FM and Fluorescence (Micro-)Spectroscopy

Tartary buckwheat grain sections were imaged with an AxioImager Z.1 (Zeiss, Oberkochen, Germany) microscope using reflected light without the coverslip and photographed with an AxioCam HRc camera (Zeiss, Oberkochen, Germany). In addition, autofluorescence of sections was imaged using a MZFLIII stereomicroscope (Leica, Wetzlar,

Table 1. Complementary Methods Selected for Imaging of a Tartary Buckwheat Grain Cross Sections and Their Main Characteristics, Advantages, and Disadvantages.

Method	Information	Spatial Resolution	Detection Limit	Advantages and Technological Readiness	Disadvantages	Result
Fluorescence (micro)spectroscopy	Structural detail Autofluorescence Quantitative	1 μm	Limited by probe and background	Localization of structural molecules and metabolites with autofluorescence	Only for fluorescing molecules	Presence of condensed tannin in endosperm
Mega electron volt- secondary ion mass spectroscopy (MeV-SIMS)	Secondary metabolites Qualitative	5–10 μm	<1% weight	Low level of fragmentation; detection of major secondary metabolites	Poor energy sensitivity, limitations to maximal energy detection	Localization of rutin and quercetin in embryonal tissues
Micro-particle Induced X-ray emission (micro-PIXE)	Elemental composition Quantitative	<1–7 μm	<1–100 mg kg^{-1}	High sensitivity for mid-Z elements	Overlapping peaks, deconvolution required Trace elements not detected	Lateral distribution of elements in embryonal tissue and the husk Co.-localization of elements and P in cotyledons
Scanning electron microscopy-energy dispersive X-ray spectroscopy (SEM-EDS)	Structural details, element composition Quantitative	<<1 μm	<0.1% weight	High spatial resolution accompanied by elemental composition (only major elements)		
Laser ablation-inductively coupled plasma mass spectrometry (LA-ICP-MS)	Element composition Qualitative	>5 μm	<0.1 mg kg^{-1}	High sensitivity for trace elements, isotope distinction	Sample damage, flatness of the sample required	Presence of light pollutants (Al) in the husk

Germany) with a Plan Apo 1.0× objective with three different epifluorescence excitation wavelengths, namely, 395–455 nm (emission light 480 nm), 490–510 nm (emission 520–550 nm), and 540–580 (emission 592–667 nm), without a coverslip. These images were recorded with a Leica DFC425C color camera as RGB TIFFs (frame size 2,592 × 1,944 px).

Fluorescence microspectroscopy was used to capture fluorescence spectra of the Tartary buckwheat grain tissues (prior to all analyses and after) and reference standards (rutin hydrate, quercetin, catechin, ferulic acid [all Sigma-Aldrich, Burlington, USA], and starch [Merck, Darmstadt, Germany]). All samples were covered with a 1.5# cover glass and imaged by an inverted microscope Axio Observer Z1, LSM 800 (Zeiss, Germany), operated by ZEN 2.6 software, using the lambda stack function. The spectral resolution was set to 20 nm (standards) or 9 nm (samples) and 405 nm laser light for excitation. In this setting, the variable dichroic mirror is sequentially shifted so that the split wavelength of fluorescent light shared between the two GaAsP-Pmt detectors is shifted for a set spectral resolution after each acquisition step. The final acquisition result is the stack of images from both detectors (lambda-stack), where each image contains fluorescence light of a limited wavelength range. By subtracting the fluorescence intensities of two images obtained in two consecutive steps, one can obtain the fluorescence intensity in the predefined spectral resolution. Although the GaAsP-Pmt detectors are sensitive to light from 400 to 700 nm, not all the emission light in this spectrum reaches them. This is due to the LSM 800 design, in which a fixed main beam splitter blocks the reflected excitation light from four available laser lines (405, 488, 561, and 640 nm), generating "blind spots" on the detector. To circumvent this obstacle, transmittance/reflectance data provided by the microscope manufacturer were taken into account, and the intensities of emitted light at wavelength intervals corresponding to detector "blind spots" were omitted in the graphs of fluorescence spectra. The intensities of emitted light at wavelength intervals that partially overlapped with "blind spots" were corrected by calculating the total transmittance factors. The objective used was EC Plan-Neofluar 10x/0.3 NA. Pinhole size was set to 1 AU. Frame size was set to 1,024 × 1,024 pixels with 12-bit depth. Frame time was 10 s. The acquired lambda stack was processed by Fiji software (Schindelin et al., 2012). The mean pixel intensity was extracted from the region of interest of 200 × 200 pixels in size from the lambda stack of raw images. The obtained pixel intensities from images obtained in sequential steps in the lambda scan were then subtracted in MS Excel to obtain the fluorescent intensities with 20 nm spectral resolution. To test for statistical significance between different pairs of fluorescence spectra in fluorescence microspectroscopy, the modified χ^2 method was applied as described by Hristova and Wimley (2023). p-value ≤ 0.05 was considered statistically significant. The means and standard errors of each of the measurement points in the fluorescence spectra of the grains were calculated from three replicates based on different regions of two to three individual grains.

Metabolite Distribution Imaging Using MeV-SIMS

Molecular distribution imaging of Tartary buckwheat grain cross-section was performed by 5 MeV Cl^{5+} primary ions, focused to a 10 μm spot size, which bombarded the surface of the sample across the 2,000 × 2,000 μm^2 scan size to desorb secondary molecules. Among those, positively ionized particles were accelerated with a 5 kV bias voltage and analyzed in a linear time-of-flight mass spectrometer, whose characteristics have been described in detail previously (Jeromel et al., 2014). Each sample was analyzed for 8 h at a beam intensity of 5,000 ions s^{-1}, corresponding to a beam fluence of 5×10^9 ions cm^{-2}, much below the static SIMS limit (10^{12} ions cm^{-2}) to prevent any significant chemical alteration. For the comparison between different measurements, all spectra were normalized to the intensity of the potassium (K) peak.

The identification of biomolecules in the sample was performed by the analysis of the reference standards of rutin-hydrate and quercetin (both Sigma-Aldrich). Both standards were dissolved in methanol (1 mg mL^{-1}), and approximately 30 μL of each was deposited on a polished Si wafer and spin-coated and analyzed as described previously (Jenčič et al., 2023).

Element Distribution Analysis at Micrometer Scale Using Micro-PIXE

Element distribution imaging of the Tartary buckwheat grain cross-sections was performed at the nuclear microprobe of the Jožef Stefan Institute, Ljubljana, Slovenia, as described in detail previously (Pongrac et al., 2011; Lyubenova et al., 2012). In short, protons with 3 MeV energy were focused to a beam of approximately 1 × 1 μm^2. The proton beam was raster scanned over a 2,000 × 2,000 μm^2 large sample area yielding 1.8588 μC total proton dose in the measurement lasting 6.25 h. Emitted X-rays of magnesium (Mg), phosphorus (P), sulfur (S), chlorine (Cl), K, and calcium (Ca) were detected by a Si drift detector (e2v SiriusSDVR; High Wycombe, UK) and manganese (Mn), iron (Fe), and zinc (Zn) by high purity Ge detector (Canberra Packard Central Europe GmbH, Schwadorf, Austria). Spectra were collected using OM-DAQ software (Oxford Microbeams Ltd., Oxford, UK) and processed in GeoPIXE II software (Ryan, 2000). Proton dose was determined using a rotating, in-beam chopper (Vogel-Mikuš et al., 2009). Cellulose was used as a matrix for element quantification.

Element Distribution Analysis Below Micrometer Scale Using SEM-EDS

Tartary buckwheat grain cross-sections were carbon-coated (10 nm thick layer) using a sputter coater BAL-TEC SCD 005 (BAL-TECH Inc., Balzers, Lichtenstein), and the detailed morphological makeup of the Tartary buckwheat grain was visualized using a scanning electron microscope (JEOL JSM-5800, Jeol, Ltd., Tokyo, Japan) with 20 keV beam energy at 10 mm working distance in high vacuum mode. Regions of interest (starch granules in the endosperm, globoids in the cotyledons and of the pericarp) were analyzed for element composition using Si(Li) X-ray detector (ISIS 300 EDS, Oxford Instruments plc, Abingdon, UK) with the following conditions: process time 5, acquisition time 60 s, count rate 1,000 cps, dead time 30%, and magnification of 2,700×.

Element Distribution Analysis for Elements Present at Low Concentration by LA-ICP-MS

Distribution of Al and Si (both found in common buckwheat grain below 100 $\mu g\ g^{-1}$ dry matter; Vogel-Mikuš et al., 2009) and P (found in common and Tartary buckwheat grain, much above 1,000 $\mu g\ g^{-1}$; Vogel-Mikuš et al., 2009; Pongrac et al., 2016, 2013) was determined by LA-ICP-MS (Agilent 7900x,

Agilent Technologies, Palo Alto, USA and Analyte G2, Teledyne Photon Machines Inc., Bozeman, USA). The laser ablation system contains a HelEx II 2-volume ablation cell with an integrated Aerosol Rapid Introduction System. The imaging parameters for best image quality were set at a square 10 μm beam size, 250 Hz, dosage 10, and fluence 0.52 J cm^{-2} and ICP-MS acquisition time 40 ms and dwell time of 4 ms. Sampled depth for each of the 10 pulses was between 150 and 200 nm (Mervič et al., 2024), making the technique insensitive to the 10 nm carbon layer on the sample surface applied for the SEM-EDS analysis.

Data Processing and Statistical Analysis

The main challenge in direct correlative imaging is the perfect alignment of pixels. Because samples were moved between analyses with different techniques and often to different facilities, postanalytical alignment of pixels was performed. The distribution of elements obtained with micro-PIXE was used as the baseline, and data from SEM, MeV-SIMS and LA-ICP-MS were aligned to it. Transformation of MeV-SIMS and LA-ICP MS maps was achieved through rotation, translation, and stretching using the following formulas:

$$x' = (x\ \mathrm{Cos}[\varphi] + y\ \mathrm{Sin}[\varphi] + T_x)\frac{1}{S_x},$$

$$y' = (y\ \mathrm{Cos}[\varphi] - y\ \mathrm{Sin}[\varphi] + T_y)\frac{1}{S_y},$$

where x' and y' were new positions of pixels x and y from the center of the image (ranging from −128 to +127 for 256 × 256 pixel maps), φ is the rotation angle on x–y plane, $T_{x,y}$ was the translation in x/y axis, and $S_{x,y}$ was stretched in x/y direction.

Twelve characteristic points of all maps (micro-PIXE, MeV-SIMS, and LA-ICP MS) were considered to determine optimal values of five parameters through the least squares method. Optimal values were determined with a precision of 1 pixel for $T_{x,y}$, $\pi/256$ π for φ, and 0.01 for $S_{x,y}$.

The final values for MeV-SIMS-PIXE conversion were $\varphi = \frac{-7\pi}{256}$, $T_x = 25$, $T_y = -1$, $S_x = 1.17$, and $S_y = 0.71$. Since Mev-SIMS measured the sample rotated 53° in regard to the primary ion beam, this led to x axis being stretched by 1/Cos (53°) = approximately 1.66. The value of the ratio S_x/S_y was similar at 1.65, indicating the squeezing/stretching of the image was solely due to the rotation of the sample during the measurement. Values of LA-ICP-MS–micro-PIXE conversion were $\varphi = \frac{-1\pi}{256}$, $T_x = -20$, $T_y = -22$, $S_x = 1.30$, and $S_y = 1.22$.

Once the alignment was concluded, datasets were used for multivariate statistics to distinguish grain tissues based on their full nutritional profiles. Data for P, S, K, Ca, Mn, Fe, and Zn from micro-PIXE, molecules with $m/z = 70$, 303, and 603 from MeV-SIMS and for Si and Al from LA-ICP-MS in each pixel were z-normalized (to eliminate the differences in value ranges) and statistically processed using k-means clustering with random initialization. The number of clusters was selected based on principal component analysis (PCA), in which four principal components explained 69.4% data variability, of which one was the background and three were linked with grain tissues. The PCA, the clustering analysis, and the hyperspectral image depicting tissues with distinctive nutritional profiles were generated in Orange Data Mining 3.13 software using HyperSpectra plugin (Demšar et al., 2013; Toplak et al., 2017).

In addition, morphology image (SEM) was fused with different distribution images (molecular from MeV-SIMS or elemental from micro-PIXE and LA-ICP-MS) by conversion as follows $\phi = -1\pi/256$, $T_x = -13$, $T_y = -18$, $S_x = 1.10$, and $S_y = 1.07$. Raw data (matrices of the SEM image and the distributions of molecules and elements) to generate custom combination(s) are available in .csv format at https://doi.org/10.5281/zenodo.14628251. Fusion of selected matrices can be conducted in the Wolfram Mathematica (Wolfram Research Inc., Champaign, IL, USA) program, where the user should provide paths of two raw datasets selected to be fused and start the program by the selection of the first (overlay) image and the second (base) image. The opacity of the first image can be adjusted so that the best visualization of the combination is achieved. Alternatively, overlay images can be generated in freely available Fiji software (Schindelin et al., 2012; https://imagej.net/software/fiji/downloads) by File > Import > Text Image to open selected matrices, followed by Image > Color > Merge Channels where SEM image, if used as the basis for morphology, could be selected as gray channel (C4), and other matrices in selected (color-specific) channels (up to 6 additional). In the Merge Channels options, "Create composite," "Keep source images," and "Ignore source LUTs" should be checked.

Results and Discussion

BFM, Autofluorescence Microscopy, and Fluorescence Spectroscopy

In a cross-section, Tartary buckwheat grain is of triangular shape (Fig. 1). It is filled with endosperm, distinctly white

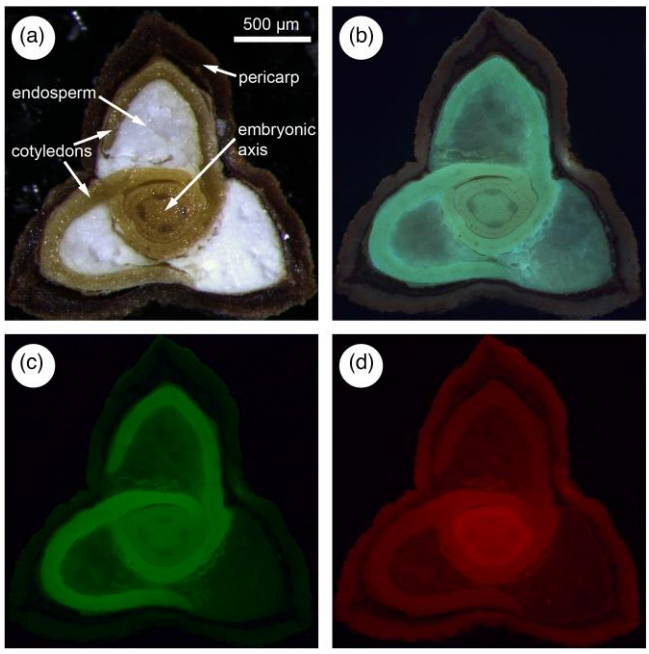

Fig. 1. Microscopy of a cross-section of a Tartary buckwheat (*F. tataricum*) grain. Bright-field stereomicroscopy image with grain tissues labeled (**a**) and the micrographs obtained with excitation light of 395–455 nm (emission light 480 nm) (**b**), 490–510 nm (emission 520–550 nm) (**c**), and 540–580 (emission 592–667 nm) (**d**) indicating the presence of diverse fluorophores in specific grain tissues.

under stereomicroscope, partially encircled with two elongated and winding cotyledons, light brown under stereomicroscope. These not-yet functional cotyledons, which contain underdeveloped etiolated chloroplasts and protochlorophyllide, are attached to the light-brown semicircular shape in the center of the grain, the embryonal axis (i.e., embryo proper). It comprises the outer cortical region and the inner pith divided by vascular cambium and four equidistantly placed vascular bundles. The endosperm, cotyledons, and embryonal axis are embedded in a dark brown multilayered husk (pericarp).

The autofluorescence images indicate diverse fluorophores in tissues of Tartary buckwheat grain, depending on the excitation wavelengths (Figs. 1b–1d), based on their autofluorescence (Table 1). The cotyledons show the most intense autofluorescence under blue light (emission at 480 nm; Fig. 1b) and green light (emission at 520–550 nm), followed by the embryonal axis. At the same time, a faint fluorescence signal is observed in the husk (Fig. 1c). Under red light, however, the embryonal axis shows the most intensive autofluorescence signal followed by autofluorescence of lower intensity in cotyledons, indicating differences in the main fluorophores in these two tissues and husk (Fig. 1d). Endosperm exhibits the lowest fluorescence signal under all conditions. The emission spectra of the diverse fluorophores in plant foods have characteristic fingerprints and are of great potential for food characterization. However, the high complexity of foods hinders the analyses, as the conventional fluorescence measurements often provide too little information for more detailed analyses, and the frequently overlapping emission spectra of the fluorophores make their identification difficult (Lenhardt et al., 2017). The most common endogenous fluorophores in green parts of plants are chlorophylls (red fluorescence upon UV excitation), followed by cell wall phenolics, intracellular ferulates (blue-green fluorescence upon UV excitation), and flavonoids (green fluorescence upon UV excitation), as reviewed in detail elsewhere (Buschmann et al., 2000; Donaldson, 2020).

Fluorescence microspectroscopy with excitation light of 405 nm captured tissue-specific differences in autofluorescence peaks in Tartary buckwheat grain cross-section (Fig. 2a). The analyses of buckwheat tissues were performed before and after other imaging methods to record the potential tissue damage or biochemical transformation of the fluorophores. No change in the fluorescence spectra of the husk, tissue with the lower water content and abundance of catechin, was observed. In contrast, in the cotyledon and endosperm, slightly lower fluorescence spectra in the 500–540 nm range were accompanied by a minute rise in the fluorescence spectra in the 580–600 nm range (Fig. 2a, 1–3), indicative of little or no radiation damage. The reference standard biomolecules had distinct fluorescence profiles (Fig. 2b) and were selected based on the large dataset of phenolic compounds identified in common buckwheat grain using high-performance liquid chromatography combined with MS/MS analysis including catechin, epicatechin gallate, orientin/isoorientin, vitexin/isovitexin, hyperin, and rutin, while quercetin was only detected in Tartary buckwheat (Zhang et al., 2017). In the cotyledon of Tartary buckwheat, the most prominent peak occurred at 518 nm (Fig. 2a, 1). A similar peak at 509–527 nm also characterized the husk (Fig. 2a, 2). Although much broader, the catechin reference standard, with a peak at 501–540 nm (Fig. 2b), was at the same wavelength. According to some reports, the major biomolecules detected in Tartary buckwheat husk were rutin and quercetin, but not catechin (Lee et al., 2016). The fluorescence signal of the rutin reference standard was very low (not shown); thus, its presence in cotyledons cannot be seen. The fluorescence properties of quercetin standard at 580–600 nm may have contributed to the fluorescence spectra of cotyledon and husk, but they are not the major fluorophore in these tissues. Some authors argue that the high fluorescence property of quercetin may stem from albumin-bound quercetin (Poór et al., 2018). In contrast, a recent comprehensive metabolome analysis revealed six proanthocyanidin molecules (catechin-based condensed tannins) with the highest concentrations in Tartary buckwheat bran, followed by endosperm and pericarp (Xiao et al., 2022), thus confirming their presence in these tissues. A more flattened peak around 536 nm was characteristic of the endosperm (Fig. 2a, 3), with no apparent connection to the peak at 501 nm observed for the starch reference standard material (Fig. 2b). Note that starch, as a polysaccharide, has no fluorochromes. The observed starch fluorescence in the reference standard indicates the presence of some fluorescent impurities. Therefore, the absence of a peak at 501 nm in the endosperm does not imply the absence of starch in this tissue. Rather, the autofluorescence properties of the Tartary buckwheat endosperm can indicate the presence of condensed tannins.

Blue-green fluorescence is derived from ferulic acid, covalently bound to most cell walls in leaves. In contrast, other phenolic acids and extractable flavonoids of the vacuoles contribute little to the fluorescence of leaves in this region (Lichtenthaler & Schweiger, 1998). Ferulic acid is also a prominent component of the nonendosperm wheat milling fractions, while in the starchy endosperm, only minute amounts are present (Pussayanawin et al., 1988). Indeed, the reference standard of ferulic acid shows weak fluorescence intensity and a peak at 460 nm (Fig. 2b), which may have contributed to the fluorescence in the blue region of the spectra in the selected Tartary buckwheat grain tissues (Fig. 2a), but not as one of the major peak components.

The spatial distribution of fluorophores in tissues of buckwheat grain is, to the best of our knowledge, underexplored. However, the profiles of fluorescent spectra of buckwheat flours are characteristic enough to allow for the determination of the quality of buckwheat noodles (Shibata et al., 2011), while coupled with parallel factor modeling, the fluorescence fingerprints proved distinctive enough to allow for the characterization of flours of differing botanical origins (Lenhardt et al., 2017).

Metabolite Identification and Imaging Using MeV-SIMS

MeV-SIMS imaging provides mass-resolving power and mass accuracy, can generate distribution maps at a submicrometer spatial resolution (Table 1), and can inform problems of interest at different dimensional scales (Anderton & Gamble, 2016) and for different scientific fields, including the food production sector. As in any MSI-based technique, detection of positively charged molecules commonly occurs in protonated or cationized form; i.e., proton or cation is attached to the (fragment of) a molecule. This results in a shift of quasi-molecular peaks by the mass of an attached agent. The cumulative MeV-SIMS spectrum of the Tartary buckwheat grain

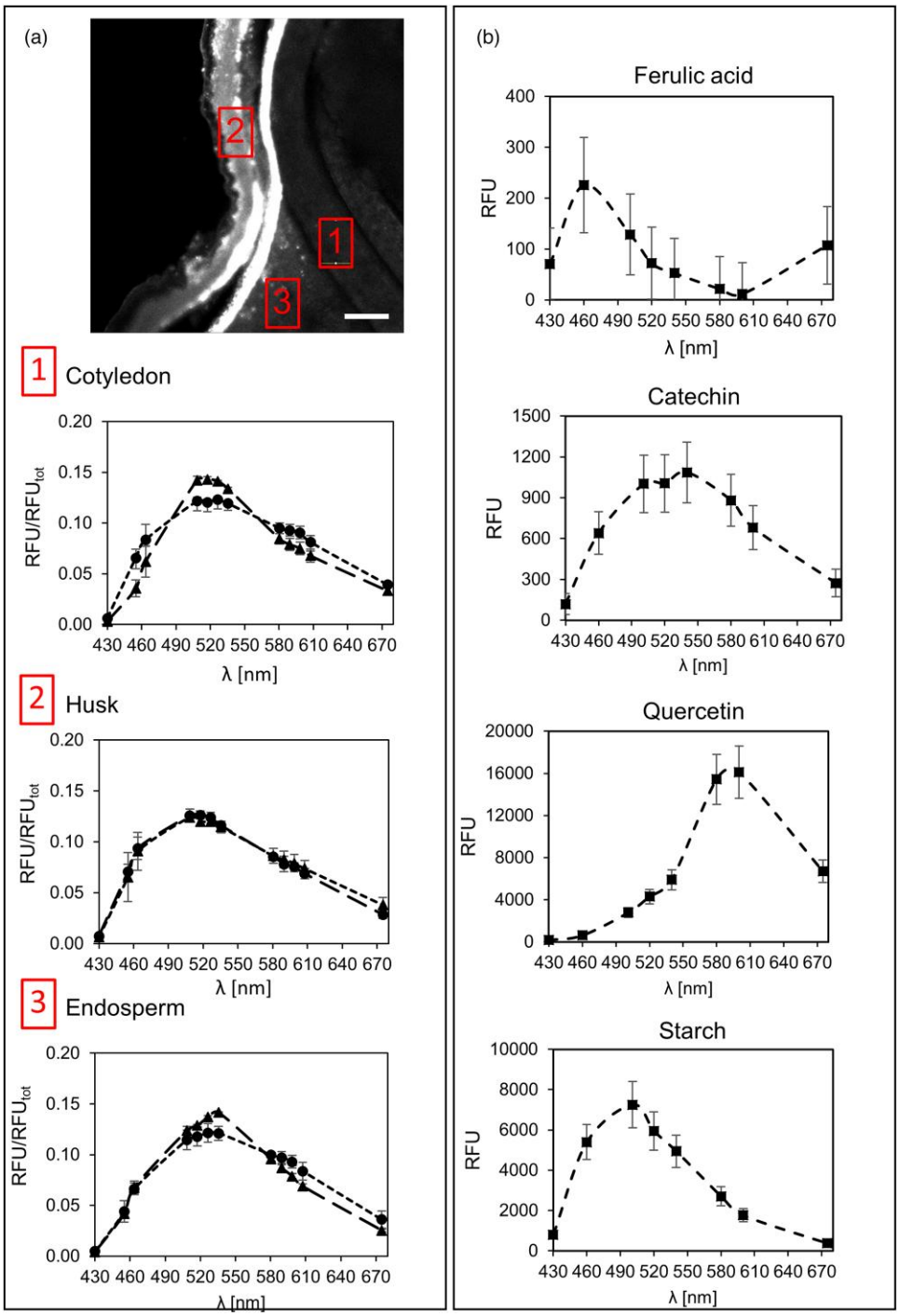

Fig. 2. Fluorescence (micro-)spectroscopy of tissues of a Tartary buckwheat (*F. tataricum*) grain (**a**) and reference standard biomolecules (**b**). Characteristic spectra of selected tissues (cotyledon, husk, and endosperm) and reference standard spectra of the expected biomolecules for comparison were obtained using excitation light at 405 nm. RFU/RFU$_{tot}$, relative fluorescence units normalized on total fluorescence of the spectrum (± standard deviation). (▲), pre-imaging grain; (●), post-imaging grain. Scale bar is 200 μm.

cross-section can be separated into two domains: the first one (up to 300 *m/z*) contains numerous elemental and/ or fragment peaks, and the second domain (between 300 and 900 *m/z*) contains fewer peaks of lower intensities (Fig. 3a). Two most prominent peaks, namely, at $m/z = 303$ and $m/z = 603$ in the second domain, were studied in more detail. Their distribution in the grain is displayed in Figure 3b. Peaks in this domain of the cumulative spectrum were compared to the MeV-SIMS spectra of reference standards (Fig. 3c), rutin ($m = 610$ Da) and quercetin ($m = 302$ Da), expected to be abundant in Tartary buckwheat grain (Fabjan et al., 2003). Allocation to cotyledons but also to endosperm was evident for quercetin, corroborating results with FM (compare with spectra in Fig. 2), whose spectrum contained a protonated molecular peak at $m/z = 303$ and several others, which represent other combinations of cationization, for example, a peak at $m/z =$ 325, 341, 347, and 381 representing quercetin + Na, quercetin + K, quercetin + COOH, and quercetin + 2Na–H,

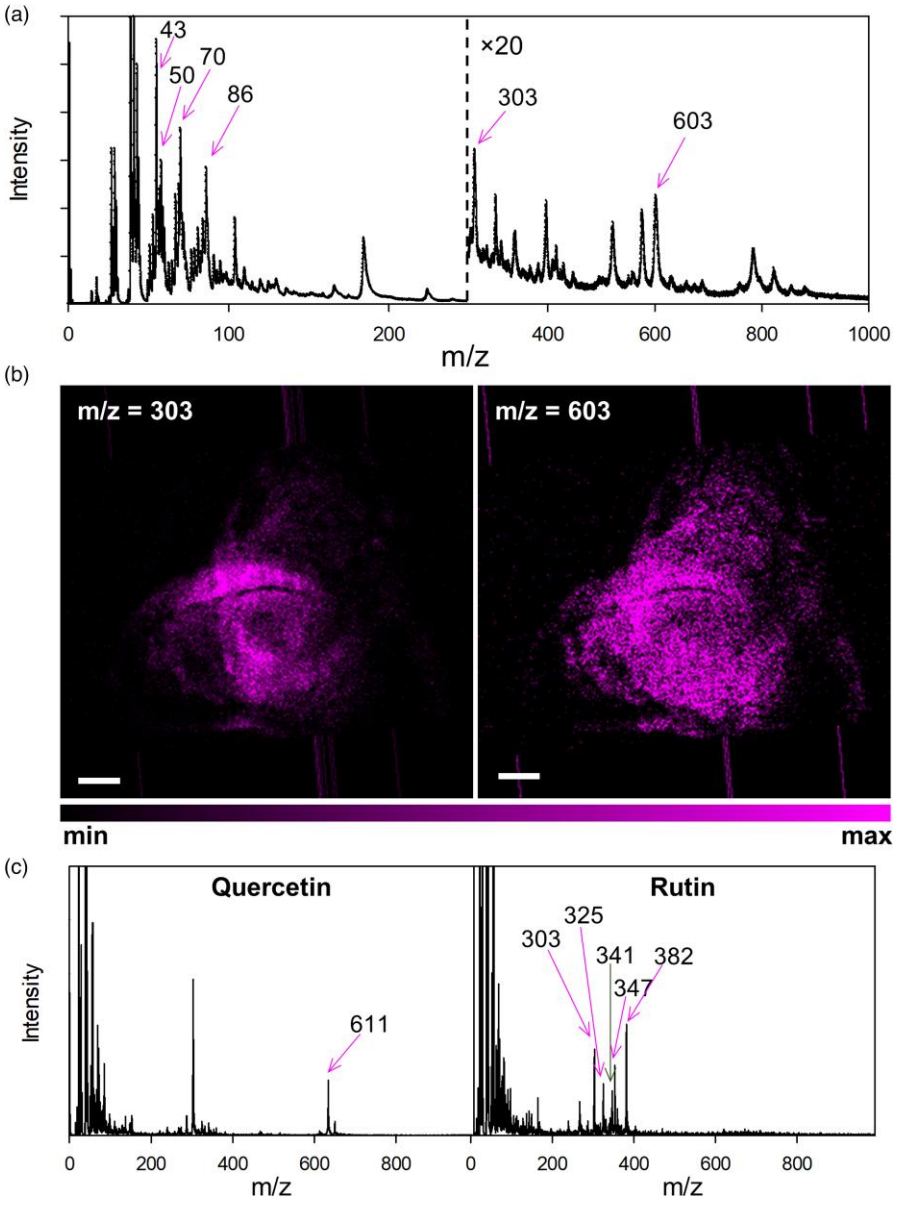

Fig. 3. MeV-SIMS analysis of a cross-section of a Tartary buckwheat (*F. tataricum*) grain. A representative cumulative MeV-SIMS spectrum with selected peaks indicated (**a**), the spatial distribution of two molecules under the selected peaks (**b**), and spectra of reference standards rutin and quercetin (**c**). The expected rutin peak at $m/z = 611$ was absent in the sample spectrum, where a prominent peak at $m/z = 603$ was observed. This molecule remains unidentified. The intensity legend represents counts s^{-1}. Scale bar is 200 μm.

respectively. By contrast, the molecule at the $m/z = 603$ exhibiting clear allocation to the embryonal axis and the cotyledons (Fig. 3b), cannot be identified as rutin, as the spectrum of the rutin standard contains peaks at $m/z = 633$ representing rutin + Na, at $m/z = 649$ representing rutin + K and at $m/z = 611$ representing rutin + H (Fig. 3c), some of which are seen only as small peaks in the MeV-SIMS spectrum of Tartary buckwheat grain (Figs. 3a, 3c). This was surprising as up to 1.7% of rutin in grain dry matter has been reported in the Tartary buckwheat grain (Fabjan et al., 2003), and intensive peaks related to rutin and rutin + M molecules were expected. It may be that peaks at $m/z = 576$ and $m/z = 603$ were related to rutin due to their prominence, similarity in mass and high correlation in their spatial distribution, but additional analyses are required to confirm this. One possible theory for the absence of rutin peaks is that the molecular composition of rutin might have altered during the sample preparation or the desorption process, most likely the disaccharide chain being disrupted at two different locations. Unfortunately, MeV-SIMS setup used did not allow for a more detailed identification of heavier molecules.

Prominent peaks in the first domain, notably at m/z values 28, 43, 55, 70, and 86. These are mostly carbohydrates ($C_2H_4^+$, $C_3H_7^+$, $C_5H_{10}^+$, and $C_6H_{14}^+$) or carbohidroxydes ($C_5H_{10}O^+$), indicative of organic tissue. The upgrade of our setup and optimization of sample handling, such as coating with a few nm thick layer of gold will enable more straightforward conclusions, as coating with gold was shown to improve secondary ion yield of already detected molecules (Jenčič et al., 2023). Furthermore, coating helps to better define the electric field at the sample, which helps with the acceleration of secondary ions and results in clearer images.

Elemental Distribution Analysis Using Micro-PIXE

Visualization and understanding of the spatial distribution of elements in plants are critical for food chemistry aiming to improve crop nutrition, productivity, nutritional contents of edible portions, or reduction of unwanted trace element contaminants (Cvitanich et al., 2011; Kopittke et al., 2020). The main parameter affecting micro-PIXE results is the penetration depth of the MeV protons, the resulting X-ray fluorescence emission and absorption of the X-ray fluorescence photons in the sample matrix. In addition, electron

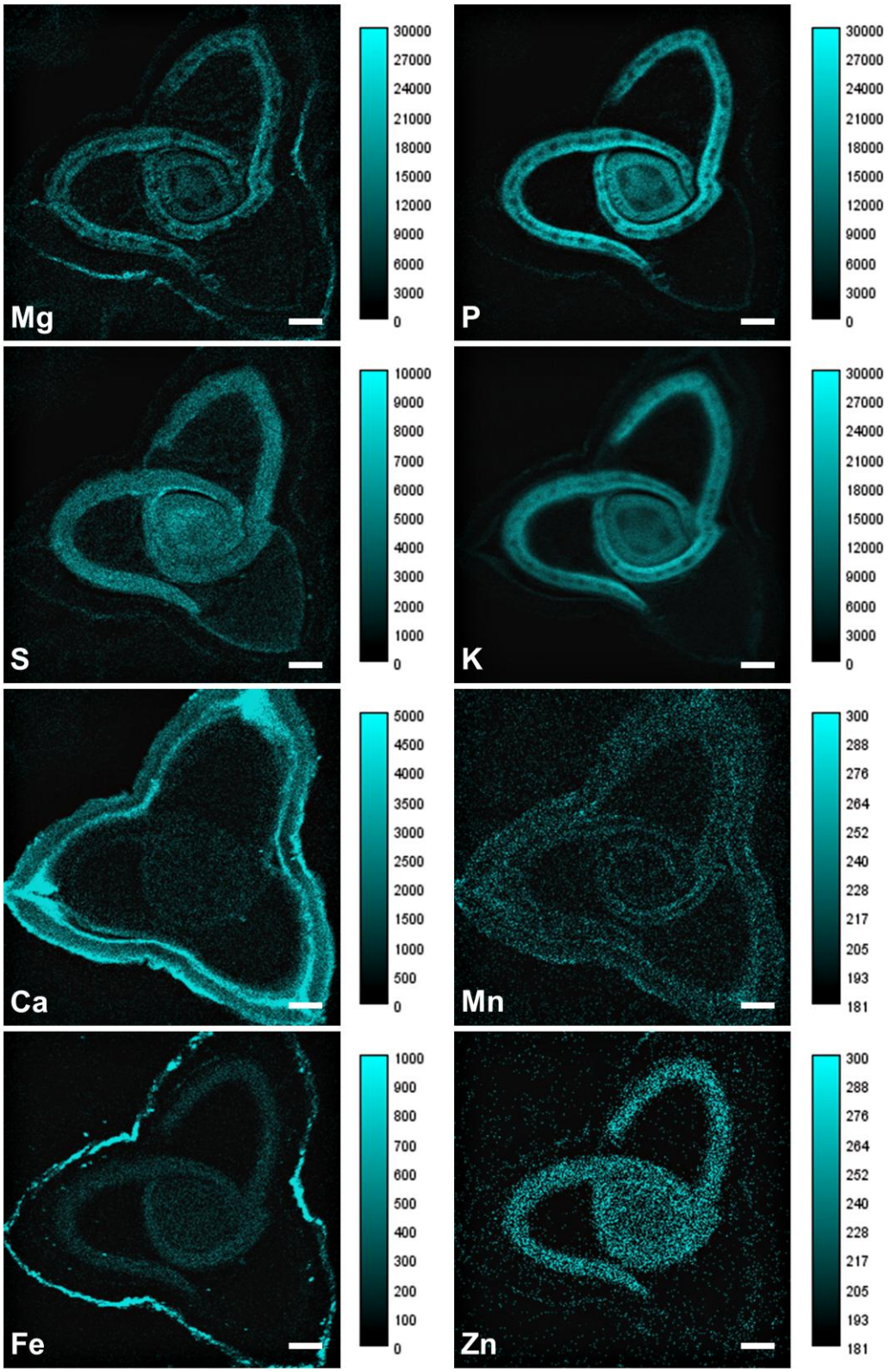

Fig. 4. Micro-PIXE analysis of a cross-section of a Tartary buckwheat (*F. tataricum*) grain. Spatial distribution maps of Mg, P, S, K, Ca, Mn, Fe, and Zn. The intensity legend next to each distribution map is in $\mu g\ g^{-1}$ dry weight. Scale bar is 200 μm.

bremsstrahlung affects sensitivity for the light elements since it increases the background in low Z region. The signals of the low Z elements (P–K) originated from the material close to the sample's surface, while the signals of the mid-Z elements came from deeper layers of the sample (Table 1). In line with previous reports on common buckwheat (Vogel-Mikuš et al., 2009; Pongrac et al., 2011) and Tartary buckwheat (Pongrac et al., 2013; 2020), most P and K were localized in the embryonal axis and the cotyledons. At the same time, prominent Ca and Fe concentrations were found in the pericarp (Fig. 4). The endosperm is not completely devoid of the measured mineral elements, although relatively lower concentrations compared to embryonal tissues may lead to such a conclusion (Fig. 4). This is the main reason for the relatively low mineral concentrations in flours, highlighting the importance of spatial analyses of mineral element composition for informative decisions in the food sector.

Subcellular Distribution of Elements Determined by SEM-EDS

A technique especially suited for forensic investigation and problem-solving in the food industry, i.e., for determining the distribution of materials within the matrix or finding organic and inorganic contaminants in food and crops, is SEM-EDS (Niemeyer, 2015) with high lateral resolution (Table 1). In addition, it is a quick and routine approach used in food sciences to image grain starch morphology (Kasem et al., 2011), and to correlate aleurone organization to conventional grain quality characters (Hands et al., 2012), among others. The aleurone layer is an essential feature of cereal grains where phytate globoids capture numerous cations (Becraft, 2007; Regvar et al., 2011). Aleurone is a vital tissue of all endosperm containing, predominantly cereal, grain. While buckwheat is botanically not a cereal, it also stores energy in a starchy endosperm. By contrast to cereals, Tartary buckwheat grain has a very reduced aleurone layer (Pongrac et al., 2013), seen as a thin layer in the bottom right corner of the S, P, and Mg micro-PIXE maps (Fig. 4). Thus, the majority of elements in Tartary buckwheat grain are allocated to the embryonal tissues, particularly to both cotyledons (Fig. 4; Pongrac et al., 2013, 2020). Despite all the knowledge accumulated, phytate globoids in cotyledons of Tartary buckwheat grain remain undescribed, therefore, SEM-EDS was used to visualize Tartary buckwheat grain tissues (Fig. 5a) and to identify and characterize globoids in the cotyledons (Fig. 5b). These were 1–2 μm large globoids, evenly distributed within the tissue and contained mostly C, O, and P, but also K, Mg, and S (Fig. 5b), confirming their role in element storage with phytate. Large endosperm cells were filled with starch granules, where some C and O are predominant elements, accompanied by minute amounts of S and K (Fig. 5c). Compared to the cotyledons, a much higher C/O ratio was observed in the endosperm and husk, indicative of dried cells in fully matured grain, resulting from programmed cell death (Golovina et al., 2000). In the multilayer pericarp, Ca accompanies C and O (Fig. 5d). These results are also in line with and complement the results obtained at the

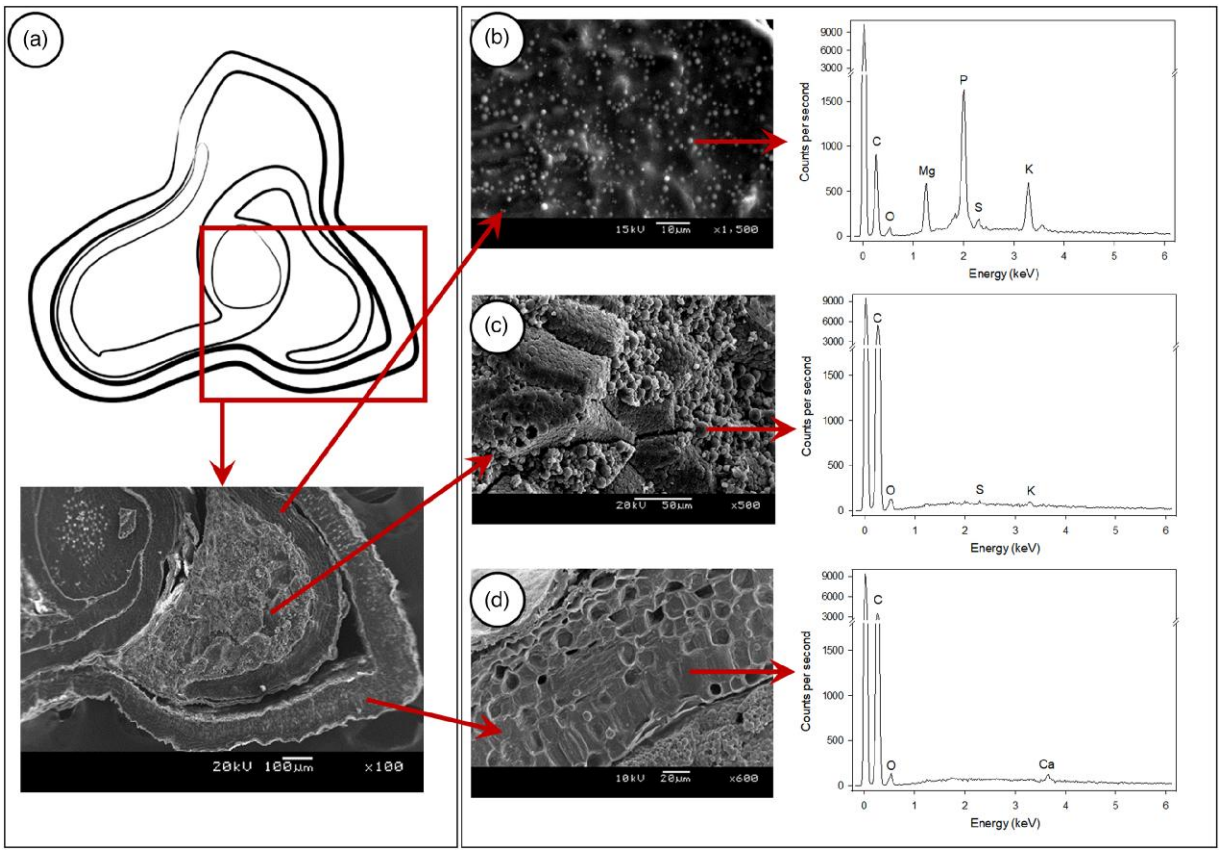

Fig. 5. SEM-EDS analysis of a cross-section of a Tartary buckwheat (*F. tataricum*) grain. The region of interest on the schematic image (highlighted with a box) and the respective scanning electron micrograph of the area (**a**) and zoomed-in on tissues with accompanying X-ray fluorescence spectra: cotyledon (**b**), endosperm (**c**), and husk (**d**). C, carbon; O, oxygen; Mg, magnesium; S, sulfur; K, potassium; Ca, calcium; keV, kilo electron volts.

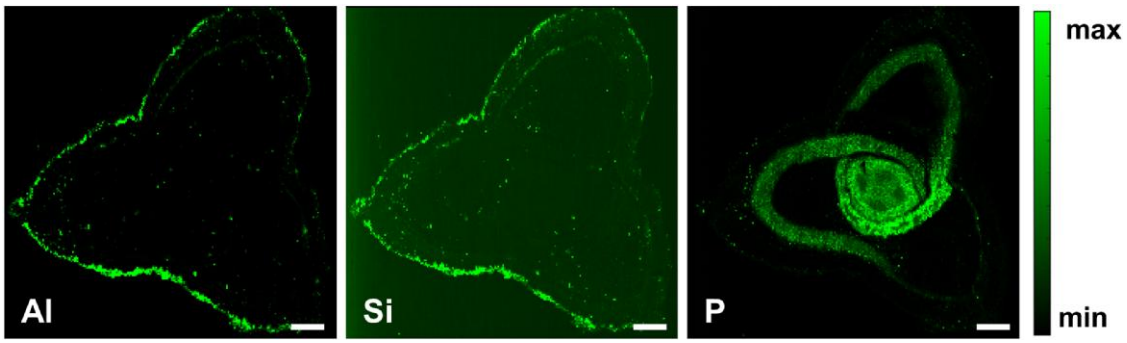

Fig. 6. LA-ICP-MS analysis of a cross-section of a Tartary buckwheat (*F. tataricum*) grain. Spatial distribution maps of non-essential elements Al and Si present at low concentrations and of an essential element P present at high concentrations (compare P distribution with results in Fig. 4). The intensity legend represents counts s^{-1}. Scale bar is 200 μm.

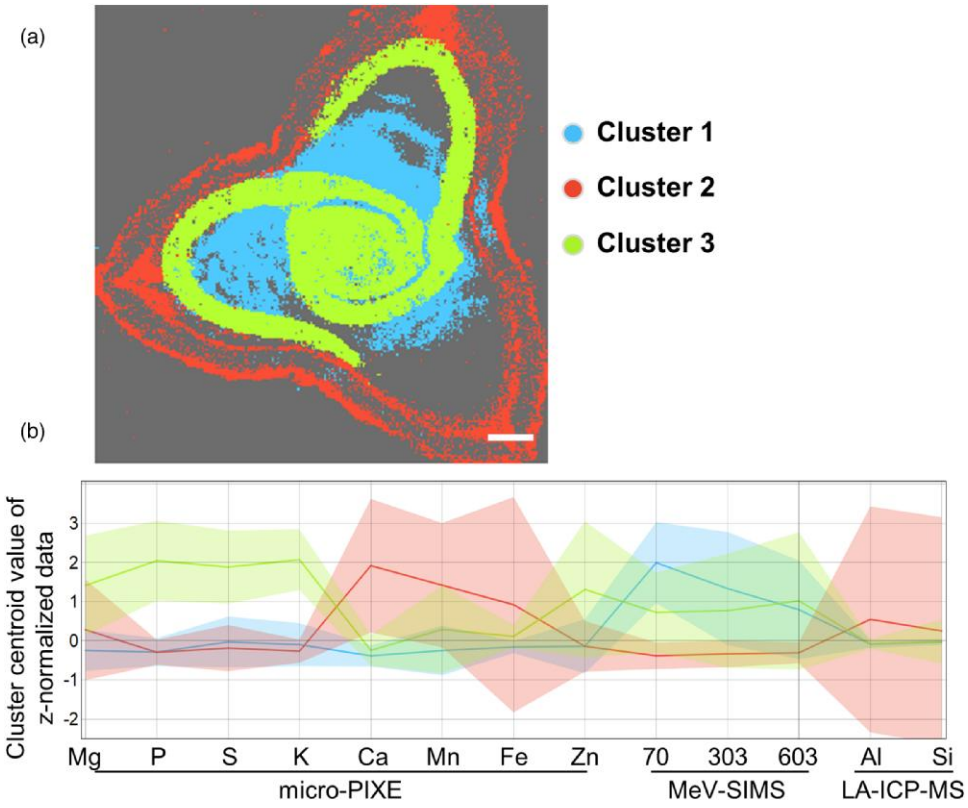

Fig. 7. Multivariate analysis for three correlative datasets (micro-PIXE, MeV-SIMS, and LA-ICP-MS) of a cross-section of a Tartary buckwheat (*F. tataricum*) grain. Image with color-coded cluster representation of *z*-normalized nutritional data coinciding with grain tissues (cotyledon with embryonal axis, endosperm, and husk) (**a**) and the nutritional profile of each cluster (**b**) depicting the three clusters in Tartary buckwheat grain explaining 69.4% of the variance of the 13 variables (eight from micro-PIXE, three from MeV-SIMS, and two from LA-ICP-MS). Scale bar is 200 μm.

smaller lateral resolution, but higher sensitivity using micro-PIXE (Fig. 4). Trace elements like Fe, Zn, and Cu were not detected in globoids due to the low sensitivity of SEM-EDS. Tartary buckwheat is a crop that performs well in poor soils and can, therefore, be regarded as an element-efficient crop plant species. An improved understanding of the structural biochemistry and elemental composition of globoids in cotyledons sheds novel insights into the mechanisms of element uptake, spatial distribution, and their physiology, allowing for the breeding of nutritionally improved crops via biofortification and is indicative of their bioavailability.

Localization of Elements Present in Small Concentrations Using LA-ICP-MS

The laser beam size used for ablation was 10 μm (square mask), and the other parameters, such as intensity, frequency, and scan speed, were optimized for the best image quality (Pessôa et al., 2017; Šala et al., 2017; van Elteren et al., 2018; Jerše et al., 2022). It is particularly suited for the analysis of heavier elements, like Hg, As, and Cd, which are hard to excite with micro-PIXE, and is also more sensitive for particular light elements like Al and Si (Table 1). The higher sensitivity of LA-ICP-MS resolves their allocation in Tartary buckwheat grain, namely, to the outer layer of the

pericarp (Fig. 6). As such, it is an excellent tool to demonstrate the presence of light element pollutants like Al in food crops. Also, the comparability of the LA-ICP-MS and micro-PIXE for elements present at higher concentrations is clearly demonstrated when P localization is considered (compare P distribution in Figs. 4, 6).

Multivariate Statistics of the Correlative Analysis

After *z*-normalization, data acquired by the sequential analyses of multiscale imaging techniques applied (micro-PIXE, MeV-SIMS, and LA-ICP-MS) were critically evaluated. The PCA of all measured Tartary buckwheat nutrients explained 69.4% of the variability of the data, returning three distinct clusters tightly linked to plant structures (Figs. 7a, 7b). Cluster 1 (in blue) primarily depicts the predominate biochemistry of the endosperm (Fig. 7a), tissue in which cluster centroid values were above average for m/z values of 70, 303, and 603, while cluster centroid values for other variables were below average (Fig. 7b). Cluster 2 (in red) depicts biochemical composition of the pericarp (Fig. 7a), a tissue in which cluster centroid values well above average for Ca, Mn, Fe, Al, and Si, while cluster centroid values for other variables were below average (Fig. 7b). Cluster 3 (in green) depicts elements and biomolecules associated with the embryonic axis and cotyledons (Fig. 7a), tissues in which centroid values were above average for Mg, P, S, K, and Zn and for m/z values of 70, 303, and 603, while cluster centroid values for other variables were below average (Fig. 7b). These results confirm a tight link between the structures composing Tartary buckwheat grain tissues and their biochemical composition (i.e., structural biochemistry) that can only be revealed using several imaging techniques in a sequential manner, on the same sample.

Fusing Morphology Image With Biochemical Information in the Research of Plant Structural Biochemistry

Finally, different correlative images can be merged to produce the most informed visualizations. For example, a montage of images was placed into a single panel (Supplementary Fig. 2). Another option is overlaying images. An SEM image was used as a morphology background, and a micro-PIXE-based K distribution map was fused to reveal the allocation of K to cotyledons (Supplementary Fused Image 1). Similarly, on the same SEM image, MeV-SIMS distribution maps under the selected peak were overlaid (Supplementary Fused Image 2). Custom combinations can be done in the Wolfram Mathematica program or in ImageJ (Merge Channels) using data available at https://doi.org/10.5281/zenodo.14628251, following the instructions in the Materials and Methods.

Conclusions

The low emission properties of fluorescence biomolecules, when excited with 405 nm light, inherently limit the information acquired using fluorescence imaging. At this excitation wavelength, catechin may be the primary fluorophore in Tartary buckwheat cotyledons in the absence of functional chlorophyll molecules inside the grain. Further detailed biomolecular identification using MeV-SIMS imaging enables access to information on the principal carbohydrate composition of organic materials and the spatial distribution of functional biomolecules of interest (e.g., quercetin). Element distribution maps of grain tissues revealed embryonal tissues and husk as major element storage within the grain. They represent an inherent advantage in conveying information on the spatial distribution of elements in question and their tissue-specific allocation, as all this complexity is revealed simultaneously and is, therefore, more straightforward to comprehend. Again, the selection of imaging techniques needs to be based on the sensitivity and spatial resolution at the required scale (Table 1). Localization of mineral elements with P indicates their immobilization by phytate. Furthermore, careful alignment of *z*-normalized values of the pixel-to-pixel integrated MSIs with elemental spatial resolution images, followed by PCA and clustering, proved highly efficient in extracting biologically meaningful information on grain biochemistry from large datasets. State-of-the-art imaging techniques, some of which are available within Euro-BioImaging platform (https://www.eurobioimaging.eu/), are of vital importance for food and agricultural sciences. Accompanied by a viable workflow, they enable novel insights into plant composition and food biochemistry and have the potential to inform decisions in combating challenges in food and nutrition of the 21st century.

Availability of Data and Materials

The authors have declared that no datasets apply for this piece.

Supplementary Material

To view supplementary material for this article, please visit https://doi.org/10.1093/mam/ozaf057.

Acknowledgments

We thank the infrastructural Centre for Electron Microscopy and Microanalysis (CEMM) of the Jožef Stefan Institute for providing access to the SEM-EDS facility. The national consortium of the Euro-BioImaging ERIC (SiMBION) is acknowledged for the provision of micro-PIXE, MeV-SIMS, LA-ICP-MS, and sample preparation facilities. We are grateful to Mr. Rangus of Rangus mlinarstvo in trgovina, Dol. Vrhpolje d.o.o., Dolenje Vrhpolje 15, 8,310 Šentjernej, Slovenia for providing Tartary buckwheat grain.

Author Contributions Statement

M.R.: investigation and writing—original draft; B.J., M.Š., A.K., M. Kobla, M. Kelemen, and P.V.: formal analysis; ID formal analysis, and visualization; K.V.-M.: funding acquisition, methodology, and writing—review & editing; I.K.: investigation; P. Pelicon: funding acquisition and resources; P. Pongrac: conceptualization, formal analysis, investigation, and writing—original draft. All authors read and approved the final version of the manuscript.

Financial Support

The authors receive financial support from the Slovenian Research and Innovation Agency (research core funding no. P1-0212, P1-0112, P1-0034, and P3-0395), project funding (J1-3014, J4-3091, J7-9398, J7-60126, N1-0090, N1-0105, and N4-0346), and infrastructure funding (I0-0005 and I0-0022-0481-0481-07).

Conflict of Interest

Authors declare there are no conflicts of interest.

References

Anderton CR & Gamble LJ (2016). Secondary ion mass spectrometry imaging of tissues, cells, and microbial systems. *Micros Today* **24**, 24–31. https://doi.org/10.1017/S1551929516000018

Becraft PW (2007). Aleurone cell development. In *Endosperm*, pp. 45–56. Berlin, Heidelberg: Springer 10.1007/7089_2007_108

Buschmann C, Langsdorf G & Lichtenthaler HK (2000). Imaging of the blue, green, and red fluorescence emission of plants: An overview. *Photosynthetica* **38**, 483–491. https://doi.org/10.1023/A:1012440903014.html

Costa C, de Jesus J, Nikula C, Murta T, Grime GW, Palitsin V, Webb R, Goodwin RJA, Bunch J & Bailey MJ (2022). Exploring new methods to study and moderate proton beam damage for multimodal imaging on a single tissue section. *J Am Soc Mass Spectrom* **33**, 2263–2272. https://doi.org/10.1021/jasms.2c00226

Cvitanich C, Przybyłowicz WJ, Mesjasz-Przybyłowicz J, Blair MW, Astudillo C, Orłowska EE, Jurkiewicz AM, Jensen EØO & Stougaard J (2011). Micro-PIXE investigation of bean seeds to assist micronutrient biofortification. *Nucl Instruments Methods Phys Res Sect B Beam Interact Mater Atoms* **269**, 2297–2302. https://doi.org/10.1016/j.nimb.2011.02.047

da Silva LC, Oliva MA, Azevedo AA & Araújo JM (2006). Responses of restinga plant species to pollution from an iron pelletization factory. *Water Air Soil Pollut* **175**, 241–256. https://doi.org/10.1007/s11270-006-9135-9

Demšar J, Curk T, Erjavec A, Hočevar T, Milutinovič M, Možina M, Polajnar M, Toplak M, Starič A, Stajdohar M, Umek L, Zagar L, Zbontar J, Zitnik M & Zupan B (2013). Orange: Data mining toolbox in Python. *J Mach Learn Res* **14**, 23492353.

Donaldson L (2020). Autofluorescence in plants. *Molecules* **25**, 2393. https://doi.org/10.3390/molecules25102393

Eckardt NA (2011). Plant science in the service of human health and nutrition. *Plant Cell* **23**, 2476–2476. https://doi.org/10.1105/tpc.111.230715

Etalo DW, De Vos RCH, Joosten MHAJ & Hall RD (2015). Spatially resolved plant metabolomics: Some potentials and limitations of laser-ablation electrospray ionization mass spectrometry metabolite imaging. *Plant Physiol* **169**, 1424–1435. https://doi.org/10.1104/pp.15.01176

Fabjan N, Rode J, Košir IJ, Wang Z, Zhang Z & Kreft I (2003). Tartary Buckwheat (*Fagopyrum tataricum* Gaertn.) as a source of dietary rutin and quercitrin. *J Agric Food Chem* **51**, 6452–6455. https://doi.org/10.1021/jf034543e

Giménez-Bastida JA & Zieliński H (2015). Buckwheat as a functional food and its effects on health. *J Agric Food Chem* **63**, 7896–7913. https://doi.org/10.1021/acs.jafc.5b02498

Golovina EA, Hoekstra FA & van Aelst AC (2000). Programmed cell death or desiccation tolerance: Two possible routes for wheat endosperm cells. *Seed Sci Res* **10**(3), 365–379. https://doi.org/10.1017/S0960258500000404

Hamany Djande CY, Pretorius C, Tugizimana F, Piater LA & Dubery IA (2020). Metabolomics: A tool for cultivar phenotyping and investigation of grain crops. *Agronomy* **10**, 831. https://doi.org/10.3390/agronomy10060831

Hands P, Kourmpetli S, Sharples D, Harris RG & Drea S (2012). Analysis of grain characters in temperate grasses reveals distinctive patterns of endosperm organization associated with grain shape. *J Exp Bot* **63**, 6253–6266. https://doi.org/10.1093/jxb/ers281

Hristova K & Wimley WC (2023). Determining the statistical significance of the difference between arbitrary curves: A spreadsheet method. *PLoS One* **18**(10), e0289619. https://doi.org/10.1371/journal.pone.0289619

Jahn KA, Barton DA, Kobayashi K, Ratinac KR, Overall RL & Braet F (2012). Correlative microscopy: Providing new understanding in the biomedical and plant sciences. *Micron* **43**, 565–582. https://doi.org/10.1016/j.micron.2011.12.004

Jenčič B, Jeromel L, Ogrinc Potočnik N, Vogel-Mikuš K, Kovačec E, Regvar M, Siketić Z, Vavpetič P, Rupnik Z, Bučar K, Kelemen M, Kovač J & Pelicon P (2016). Molecular imaging of cannabis leaf tissue with MeV-SIMS method. *Nucl Instruments Methods Phys Res Sect B Beam Interact Mater Atoms* **371**, 205–210. https://doi.org/10.1016/j.nimb.2015.10.047

Jenčič B, Pongrac P, Vasić M, Starič P, Kelemen M & Regvar M (2023). Gold-assisted molecular imaging of organic tissue by MeV secondary ion mass spectrometry. *J Am Soc Mass Spectrom* **34**, 2358–2364. https://doi.org/10.1021/jasms.3c00237

Jenčič B, Vavpetič P, Kelemen M, Vencelj M, Vogel-Mikuš K, Kavčič A & Pelicon P (2019). MeV-SIMS TOF imaging of organic tissue with continuous primary beam. *J Am Soc Mass Spectrom* **30**, 1801–1812. https://doi.org/10.1007/s13361-019-02258-8

Jeromel L, Siketić Z, Ogrinc Potočnik N, Vavpetič P, Rupnik Z, Bučar K & Pelicon P (2014). Development of mass spectrometry by high energy focused heavy ion beam: MeV SIMS with 8 MeV Cl7+ beam. *Nucl Instruments Methods Phys Res Sect B Beam Interact Mater Atoms* **332**, 22–27. https://doi.org/10.1016/j.nimb.2014.02.022

Jerše A, Mervič K, van Elteren JT, Šelih VS & Šala M (2022). Quantification anomalies in single pulse LA-ICP-MS analysis associated with laser fluence and beam size. *Analyst* **147**, 5293–5299. https://doi.org/10.1039/D2AN01172G

Kasem S, Waters DLE, Rice NF, Shapter FM & Henry RJ (2011). The endosperm morphology of rice and its wild relatives as observed by scanning electron microscopy. *Rice* **4**, 12–20. https://doi.org/10.1007/s12284-011-9060-4

Khoo CS & Knorr D (2014). Grand challenges in nutrition and food science technology. *Front Nutr* **1**, 4–3. https://doi.org/10.3389/fnut.2014.00004

Kopittke PM, Lombi E, van der Ent A, Wang P, Laird JS, Moore KL, Persson DP & Husted S (2020). Methods to visualize elements in plants. *Plant Physiol* **182**, 1869–1882. https://doi.org/10.1104/pp.19.01306

Kranjc E, Mazej D, Regvar M, Drobne D & Remškar M (2018). Foliar surface free energy affects platinum nanoparticle adhesion, uptake, and translocation from leaves to roots in arugula and escarole. *Environ Sci Nano* **5**, 520–532. https://doi.org/10.1039/C7EN00887B

Lee L-S, Choi E-J, Kim C-H, Sung J-M, Kim Y-B, Seo D-H, Choi H-W, Choi Y-S, Kum J-S & Park J-D (2016). Contribution of flavonoids to the antioxidant properties of common and Tartary buckwheat. *J Cereal Sci* **68**, 181–186. https://doi.org/10.1016/j.jcs.2015.07.005

Lenhardt L, Zeković I, Dramićanin T, Milićević B, Burojević J & Dramićanin MD (2017). Characterization of cereal flours by fluorescence spectroscopy coupled with PARAFAC. *Food Chem* **229**, 165–171. https://doi.org/10.1016/j.foodchem.2017.02.070

Lichtenthaler HK & Schweiger J (1998). Cell wall bound ferulic acid, the major substance of the blue-green fluorescence emission of plants. *J Plant Physiol* **152**, 272–282. https://doi.org/10.1016/S0176-1617(98)80142-9

Lippold E, Schlüter S, Mueller CW, Höschen C, Harrington G, Kilian R, Gocke MI, Lehndorff E, Mikutta R & Vetterlein D (2023). Correlative imaging of the rhizosphere—A multimethod workflow for targeted mapping of chemical gradients. *Environ Sci Technol* **57**, 1538–1549. https://doi.org/10.1021/acs.est.2c07340

Luo K, Zhou X & Zhang G (2019). The impact of Tartary buckwheat extract on the nutritional property of starch in a whole grain context. *J Cereal Sci* **89**, 102798. https://doi.org/10.1016/j.jcs.2019.102798

Lyubenova L, Pongrac P, Vogel-Mikuš K, Mezek GK, Vavpetič P, Grlj N, Kump P, Nečemer M, Regvar M, Pelicon P & Schröder P (2012). Localization and quantification of Pb and nutrients in *Typha latifolia* by micro-PIXE. *Metallomics* **4**, 333–341. https://doi.org/10.1039/c2mt00179a

Mayer A-MB, Trenchard L & Rayns F (2022). Historical changes in the mineral content of fruit and vegetables in the UK from 1940 to 2019: A concern for human nutrition and agriculture. *Int J Food Sci Nutr* **73**, 315–326. https://doi.org/10.1080/09637486.2021.1981831

Mervič K, Šelih VS, Šala M & Van Elteren JT (2024). Non-matrix-matched calibration in bulk multi-element laser ablation–inductively coupled plasma–mass spectrometry analysis of diverse materials. *Talanta* **271**, 125712. https://doi.org/10.1016/j.talanta.2024.125712

Miner GL, Delgado JA, Ippolito JA, Johnson JJ, Kluth DL & Stewart CE (2022). Wheat grain micronutrients and relationships with yield and protein in the U. S. Central Great Plains. *Field Crops Res* **279**, 108453. https://doi.org/10.1016/j.fcr.2022.108453

Moore KL, Schröder M, Wu Z, Martin BGH, Hawes CR, McGrath SP, Hawkesford MJ, Feng Ma J, Zhao F-J & Grovenor CRM (2011). High-resolution secondary ion mass spectrometry reveals the contrasting subcellular distribution of arsenic and silicon in rice roots. *Plant Physiol* **156**, 913–924. https://doi.org/10.1104/pp.111.173088

Morishita T, Yamaguchi H & Degi K (2007). The contribution of polyphenols to antioxidative activity in common buckwheat and Tartary buckwheat grain. *Plant Prod Sci* **10**, 99–104. https://doi.org/10.1626/pps.10.99

Murphy KM, Hoagland LA, Yan L, Colley M & Jones SS (2011). Genotype × environment interactions for mineral concentration in grain of organically grown spring wheat. *Agron J* **103**, 1734–1741. https://doi.org/10.2134/agronj2011.0097

Murphy KM, Reeves PG & Jones SS (2008). Relationship between yield and mineral nutrient concentrations in historical and modern spring wheat cultivars. *Euphytica* **163**, 381–390. https://doi.org/10.1007/s10681-008-9681-x

Nakata Y, Honda Y, Ninomiya S, Seki T, Aoki T & Matsuo J (2008). Yield enhancement of molecular ions with MeV ion-induced electronic excitation. *Appl Surf Sci* **255**, 1591–1594. https://doi.org/10.1016/j.apsusc.2008.05.108

Nielsen FH (1984). Ultratrace elements in nutrition. *Annu Rev Nutr* **4**, 21–41. https://doi.org/10.1146/annurev.nu.04.070184.000321

Niemeyer WD (2015). SEM/EDS analysis for problem solving in the food industry. Proc. SPIE 9636, Scanning Microscopies 2015, 96360G. https://doi.org/10.1117/12.2196962

Pessôa GS, Lopes Júnior CA, Madrid KC & Arruda MAZ (2017). A quantitative approach for Cd, Cu, Fe and Mn through laser ablation imaging for evaluating the translocation and accumulation of metals in sunflower seeds. *Talanta* **167**, 317–324. https://doi.org/10.1016/j.talanta.2017.02.029

Pfander C, Bischof J, Childress-Poli M, Keppler A, Viale A, Aime S & Eriksson JE (2022). Euro-BioImaging—Interdisciplinary research infrastructure bringing together communities and imaging facilities to support excellent research. *iScience* **25**, 103800. https://doi.org/10.1016/j.isci.2022.103800

Pongrac P, Kelemen M, Vavpetič P, Vogel-Mikuš K, Regvar M & Pelicon P (2020). Application of micro-PIXE (particle induced X-ray emission) to study buckwheat grain structure and composition. *Fagopyrum* **37**, 5–10. https://doi.org/10.3986/fag0012

Pongrac P, Potisek M, Fraś A, Likar M, Budič B, Myszka K, Boros D, Nečemer M, Kelemen M, Vavpetič P, Pelicon P, Vogel-Mikuš K, Regvar M & Kreft I (2016). Composition of mineral elements and bioactive compounds in Tartary buckwheat and wheat sprouts as affected by natural mineral-rich water. *J Cereal Sci* **69**, 9–16. https://doi.org/10.1016/j.jcs.2016.02.002

Pongrac P, Vogel-Mikuš K, Jeromel L, Vavpetič P, Pelicon P, Kaulich B, Gianoncelli A, Eichert D, Regvar M & Kreft I (2013). Spatially resolved distributions of the mineral elements in the grain of Tartary buckwheat (*Fagopyrum tataricum*). *Food Res Int* **54**, 125–131. https://doi.org/10.1016/j.foodres.2013.06.020

Pongrac P, Vogel-Mikuš K, Regvar M, Vavpetič P, Pelicon P & Kreft I (2011). Improved lateral discrimination in screening the elemental composition of buckwheat grain by micro-PIXE. *J Agric Food Chem* **59**, 1275–1280. https://doi.org/10.1021/jf103150d

Poór M, Boda G, Kunsági-Máté S, Needs PW, Kroon PA & Lemli B (2018). Fluorescence spectroscopic evaluation of the interactions of quercetin, isorhamnetin, and quercetin-3′-sulfate with different albumins. *J Lumin* **194**, 156–163. https://doi.org/10.1016/j.jlumin.2017.10.024

Pussayanawin V, Wetzel DL & Fulcher RG (1988). Fluorescence detection and measurement of ferulic acid in wheat milling fractions by microscopy and HPLC. *J Agric Food Chem* **36**, 515–520. https://doi.org/10.1021/jf00081a027

Regvar M, Eichert D, Kaulich B, Gianoncelli A, Pongrac P, Vogel-Mikuš K & Kreft I (2011). New insights into globoids of protein storage vacuoles in wheat aleurone using synchrotron soft X-ray microscopy. *J Exp Bot* **62**, 3929–3939. https://doi.org/10.1093/jxb/err090

Ryan CG (2000). Quantitative trace element imaging using PIXE and the nuclear microprobe. *Int J Imaging Syst Technol* **11**, 219–230. https://doi.org/10.1002/ima.1007

Šala M, Šelih VS & van Elteren JT (2017). Gelatin gels as multi-element calibration standards in LA-ICP-MS bioimaging: Fabrication of homogeneous standards and micro-homogeneity testing. *Analyst* **142**, 3356–3359. https://doi.org/10.1039/C7AN01361B

Schindelin J, Arganda-Carreras I, Frise E, Kaynig V, Longair M, Pietzsch T, Preibisch S, Rueden C, Saalfeld S, Schmid B, Tinevez J-Y, White DJ, Hartenstein V, Eliceiri K, Tomancak P & Cardona A (2012). Fiji: An open-source platform for biological-image analysis. *Nat Methods* **9**(7), 676–682. https://doi.org/10.1038/nmeth.2019

Schreck E, Foucault Y, Sarret G, Sobanska S, Cécillon L, Castrec-Rouelle M, Uzu G & Dumat C (2012). Metal and metalloid foliar uptake by various plant species exposed to atmospheric industrial fallout: Mechanisms involved for lead. *Sci Total Environ* **427–428**, 253–262. https://doi.org/10.1016/j.scitotenv.2012.03.051

Shibata M, Fujita K, Sugiyama J, Tsuta M, Kokawa M, Mori Y & Sakabe H (2011). Predicting the buckwheat flour ratio for commercial dried buckwheat noodles based on the fluorescence fingerprint. *Biosci Biotechnol Biochem* **75**, 1312–1316. https://doi.org/10.1271/bbb.110091

Toplak M, Birarda G, Read S, Sandt C, Rosendahl SM, Vaccari L, Demšar J & Borondics F (2017). Infrared orange: Connecting hyperspectral data with machine learning. *Synchrotron Radiat News* **30**, 40–45. https://doi.org/10.1080/08940886.2017.1338424

van Elteren JT, Šelih VS, Šala M, Van Malderen SJM & Vanhaecke F (2018). Imaging artifacts in continuous scanning 2D LA-ICP-MS imaging due to non-synchronization issues. *Anal Chem* **90**, 2896–2901. https://doi.org/10.1021/acs.analchem.7b05134

Vavpetič P, Vogel-Mikuš K, Jeromel L, Ogrinc Potočnik N, Pongrac P, Drobne D, Pipan Tkalec Ž, Novak S, Kos M, Koren Š, Regvar M & Pelicon P (2015). Elemental distribution and sample integrity comparison of freeze-dried and frozen-hydrated biological tissue samples with nuclear microprobe. *Nucl Instruments Methods Phys Res Sect B Beam Interact Mater Atoms* **348**, 147–151. https://doi.org/10.1016/j.nimb.2015.01.063

Vogel-Mikuš K, Pongrac P & Pelicon P (2014). Micro-PIXE elemental mapping for ionome studies of crop plants. *Int J PIXE* **24**, 217–233. https://doi.org/10.1142/S0129083514400142

Vogel-Mikuš K, Pongrac P, Pelicon P, Vavpetič P, Povh B, Bothe H & Regvar M (2009). Micro-PIXE analysis for localization and quantification of elements in roots of mycorrhizal metal-tolerant plants. In *Symbiotic Fungi: Principles and Practice*, Varma A & Kharkwal AC (Eds.), pp. 227–242. Berlin, Heidelberg: Springer. https://doi.org/10.1007/978-3-540-95894-9_14

Vogel-Mikuš K, Simčič J, Pelicon P, Budnar M, Kump P, Nečemer M, Mesjasz-Przybyłowicz J, Przybyłowicz WJ & Regvar M (2008). Comparison of essential and non-essential element distribution in leaves of the Cd/Zn hyperaccumulator *Thlaspi praecox* as revealed by micro-PIXE. *Plant Cell Environ* **31**, 1484–1496. https://doi.org/10.1111/j.1365-3040.2008.01858.x

Walter A, Kleywegt GJ & Verkade P (2021). Correlative multimodal imaging: Building a community. In *Correlative Light and Electron Microscopy IV vol. 162, Methods in Cell Biology*, Müller-Reichert T, Verkade P (Eds.), pp. 417–430. Elsevier Inc.: Academic Press.

Walter A, Paul-Gilloteaux P, Plochberger B, Sefc L, Verkade P, Mannheim JG, Slezak P, Unterhuber A, Marchetti-Deschmann M, Ogris M, Bühler K, Fixler D, Geyer SH, Weninger WJ, Glösmann M, Handschuh S & Wanek T (2020). Correlated multimodal imaging in life sciences: Expanding the biomedical horizon. *Front Phys* **8**, 47. https://doi.org/10.3389/fphy.2020.00047/full

White PJ & Broadley MR (2005). Historical variation in the mineral composition of edible horticultural products. *J Horticult Sci Biotechnol* **80**, 660–667. https://doi.org/10.1080/14620316.2005.11511995

White PJ, George TS, Gregory PJ, Bengough AG, Hallett PD & McKenzie BM (2013). Matching roots to their environment. *Ann Bot* **112**, 207–222. https://doi.org/10.1093/aob/mct123

Xiao Y, Li K, Zhang H, Li Y, Han L, Liu H & Wang M (2022). The profile of buckwheat tannins based on widely targeted metabolome analysis and pharmacokinetic study of ellagitannin metabolite urolithin A. *LWT* **156**, 113069. https://doi.org/10.1016/j.lwt.2022.113069

Yamaji N & Ma JF (2019). Bioimaging of multiple elements by high-resolution LA-ICP-MS reveals altered distribution of mineral elements in the nodes of rice mutants. *Plant J* **99**, 1254–1263. https://doi.org/10.1111/tpj.14410

Zhang W, Zhu Y, Liu Q, Bao J & Liu Q (2017). Identification and quantification of polyphenols in hull, bran and endosperm of common buckwheat (Fagopyrum esculentum) seeds. *J Funct Foods* **38**, 363–369. https://doi.org/10.1016/j.jff.2017.09.024

Zhao C, Guo L, Dong J & Cai Z (2021). Mass spectrometry imaging-based multi-modal technique: Next-generation of biochemical analysis strategy. *Innovation* **2**, 100151. doi:10.1016/j.xinn.2021.100151